


ARTICLE

DOI: 10.1038/s41467-018-07102-3

OPEN

Shockwave generates $\langle 100 \rangle$ dislocation loops in bcc iron

Qing Peng ^{1,2}, Fanjiang Meng^{1,3}, Yizhong Yang^{1,3}, Chenyang Lu¹, Huiqiu Deng⁴, Lumin Wang¹
Suvranu De⁵ & Fei Gao^{1,4}

The formation mechanism of $\langle 100 \rangle$ interstitial dislocation loops in ferritic steels stemming from irradiation remains elusive, as their formations are either too short for experiments, or too long for molecular dynamics simulations. Here, we report on the formation of both interstitial and vacancy dislocation loops in high energy displacement cascades using large-scale molecular dynamics simulations with up to 220 million atoms. Riding the supersonic shockwave generated in the cascade, self-interstitial atoms are punched out to form $\langle 100 \rangle$ dislocation loops in only a few picoseconds during one single cascade event, which is several orders of magnitude faster than any existing mechanisms. The energy analysis suggests that the formation of the interstitial loops depends on kinetic energy redistribution, where higher incidence energy or larger atom mass could improve the probability of the direct nucleation of interstitial dislocation loops.

¹Nuclear Engineering and Radiological Sciences, University of Michigan, Ann Arbor, MI 48109, USA. ²School of Power and Mechanical Engineering, Wuhan University, 430072 Wuhan, China. ³Shanghai Nuclear Engineering Research and Design Institute, 200233 Shanghai, China. ⁴College of Materials Science and Engineering, Hunan University, 410082 Changsha, China. ⁵Department of Mechanical, Aerospace and Nuclear Engineering, Rensselaer Polytechnic Institute, Troy, NY 12180, USA. Correspondence and requests for materials should be addressed to Q.P. (email: qpeng.org@gmail.com) or to C.L. (email: Chenylu@umich.edu) or to H.D. (email: qdeng@hnu.edu.cn)

Alloyed iron has incomparable hardness among all metals, in part because of the high density of dislocations^{1–3}, a line defect in crystals, which can be formed by quenching, deformation, and irradiation⁴. Different types of dislocations in a crystal can be denoted by an atomic translation known as the Burgers vector. Dislocations can form 3D networks or 2D loops. Extensively consistent experiments have identified two kinds of dislocation loops, one with $\langle 100 \rangle$ and the other with $1/2 \langle 111 \rangle$ Burgers vector, in body-centred cubic (bcc) iron using transmission electron microscopy (TEM) since 1960^{5–11}. A dislocation loop can consist of interstitial atoms or vacancies¹², whereas the prismatic interstitial type dislocation loops attract more attention due to their high mobility¹. It is generally accepted that the formation energy of $\langle 100 \rangle$ loops is higher than $\langle 111 \rangle$ loops¹³, meaning that direct nucleation of $\langle 100 \rangle$ loops from interstitial atoms is highly unlikely. Although it has been suggested that the loops can be formed directly from bombardment⁸, there is no direct observation of the formations of $\langle 100 \rangle$ interstitial loops, neither from experiments nor molecular dynamics (MD) simulations in the past half century.

Five possible formation mechanisms have been proposed. We roughly denoted here as $\langle 110 \rangle$ shear, $\langle 111 \rangle$ reaction, $\langle 111 \rangle$ transformation, C15 transformation, and cascade overlapping. In 1965, Eyre and Bullough proposed that a $\langle 100 \rangle$ loop can form as a result of $1/2 \langle 1\bar{1}0 \rangle$ shear of a faulted $1/2 \langle 110 \rangle$ loop¹⁴. Although this $\langle 110 \rangle$ shear mechanism obeys the Kirchinoff law that conserves the burgers vectors, it has not been confirmed by MD simulations, as the proposed mechanism involves the formation of faulted loops, which is unfavourable due to high energy cost. Through atomistic modelling, Marian et al.¹³ proposed that two gliding $\langle 111 \rangle$ loops could meet and interact to form one $\langle 100 \rangle$ loop. Later, this loop formation was observed in Kinetic Monte Carlo simulations with stochastic components¹⁵. However, this $\langle 111 \rangle$ reaction mechanism needs stringent conditions, such as similar sizes and overlapping glide cylinders of the two colliding $\langle 111 \rangle$ loops. As a result, it is a rare event in reality¹⁶. Besides, the segments of $\langle 100 \rangle$ type dislocations formed in such a reaction mechanism are dynamically unstable and a single $\langle 111 \rangle$ dislocation loop eventually forms¹⁷. Chen et al. proposed a mechanism that $\langle 111 \rangle$ loops could transform from $\langle 111 \rangle$ loops directly at high temperatures¹⁸. They only justified it in a 4-SIA cluster, which seems to be challenging at larger sizes, since a junction has to form when the loop is partially reoriented, leading to a drastic increase in total loop length and energy. Recently, Zhang et al. proposed a mechanism that $\langle 100 \rangle$ loops can be transformed from a C15 Laves phase interstitial cluster^{19,20}. This C15 transformation mechanism was further developed by ab initio calculations based discrete-continuum model²⁰. Very recently, Granberg et al. proposed a mechanism of cascades overlapping with pre-existing radiation damage from MD simulations²¹. However, the dose rate is about nine orders of magnitude higher than that in any experiments. All these mechanisms assume thermodynamic equilibrium conditions and some precursors. Stimulations like stress²², temperature⁹, and impurities (carbon¹⁷, chromium¹¹, helium²³, etc) could change the relative stability of $\langle 100 \rangle$ over $\langle 111 \rangle$ clusters, and the rate of reaction or transformation, but not enough to explain their common occurrence of $\langle 100 \rangle$ loops under irradiation¹⁷. Nevertheless, all these proposed mechanisms require a long time (i.e. nanoseconds and above) due to the high energy barriers. In general, the energy barrier is more than tens of electronvolt for a nanometre size loop, making it infeasible to observe in the time scale of MD simulations²⁴. It is worth noting that $\langle 100 \rangle$ interstitial loops have been observed by MD simulation of a single ion impact in bcc tungsten²⁵. However, the atomic potential used for tungsten describes a $\langle 100 \rangle$ interstitial cluster to be stable than a $\langle 111 \rangle$

cluster, which is in contrast to ab initio calculations²⁶. In addition, the kinetics are totally different because of the absence of subcascades in tungsten, as opposed to iron.

Here, we propose a punch mechanism for the formation of $\langle 100 \rangle$ loops by supersonic shockwave during high energy displacement cascade in bcc iron. This process occurs very quickly, in only a few picoseconds (ps, 10^{-12} seconds). In addition, the process does not require any precursors other than point defects. These two features make it distinguishable from all previous mechanisms. The supersonic shockwave generated in the cascade^{27–29} with 0.1 picoseconds is the stimulus, offering enough energy to nucleate the $\langle 100 \rangle$ loops directly from the pure lattices within high energy displacement cascades. Comparing to vacancy-type dislocation loops, the interstitial-type loops are more interesting because they are a feature of radiation damage and key media for material degradation, including irradiation-induced swelling, hardening, and plasticity³⁰. Therefore, we focus on the self-interstitial type dislocations.

Results

Punch-out procedure. We investigate the displacement cascades in pure bcc iron via molecular dynamics simulations at a temperature of 300 K. The high Primary Knock-on Atom (PKA) recoil energy E_{PKA} of 100, 150, and 200 keV are modelled within large simulation boxes containing 16,000,000 and 221,184,000 atoms. The high energy particle starts in the $\langle 351 \rangle$ direction from the left side of the simulation box at time zero. The nucleation process of a $\langle 100 \rangle$ interstitial loop in a displacement cascade with $E_{\text{PKA}} = 200$ keV is illustrated in snapshots in Fig. 1. For clarity, only part of the simulation cell is shown. The cascade procedure starts with supersonic shock wave at the speed of 831 km s^{-1} . The initiation of the subcascades is illustrated in Fig. 1a, followed by the thermal spike shown in b. The $\langle 100 \rangle$ dislocation loop is generated right after the shock wave, as marked in c. The $\langle 100 \rangle$ loop is completely formed in d, at 13 ps after the collision and stabilized. There is no significant change in size and shape of the loop hereafter. The snapshot at time of 50 ps is in f. The whole movie is in Supplementary Movie 1. We extended our simulation time up to 1912 ps and still no much change occurs in this $\langle 100 \rangle$ interstitial loop.

We for the first time have directly observed the nucleation of the individual $\langle 100 \rangle$ interstitial loops in the displacement cascades in bcc iron. The nucleation starts right after thermal spike at 4.0 ps after the primary collision. Visible $\langle 100 \rangle$ dislocation segments are illustrated in c-f as the arrow pointed to. A complete individual $\langle 100 \rangle$ interstitial loop finally forms at 9 ps with the dislocation length of 4.4 nm. The nucleation is very fast, orders of magnitude faster than all previous proposed nucleation mechanism. This might be due to non-equilibrium process during the cascade, where high temperatures and high pressures could appear locally at the shockwave front. The dislocation length fluctuates around 4.4 nm. There is no obvious growth within our simulation time. Once the individual $\langle 100 \rangle$ interstitial loop nucleates, it is much stable compared to point defects and $\langle 111 \rangle$ dislocation loops.

Punch-out mechanism. In order to gain more insight into the formation mechanism, we examine two individual loops, one $\langle 100 \rangle$ (red) and one $\langle 111 \rangle$ (green) loop, shown in the bottom right corner of Fig. 1f. They are selected intentionally because they nucleate almost simultaneously in the same subcascade. The same formation environment makes them ideal objects to study the formation mechanism. The zoom-in figure with orientation mark is displayed in the inset of Fig. 2c. The number of interstitial atoms contained in the loop is 40 and 108 for $\langle 100 \rangle$ and $\langle 111 \rangle$

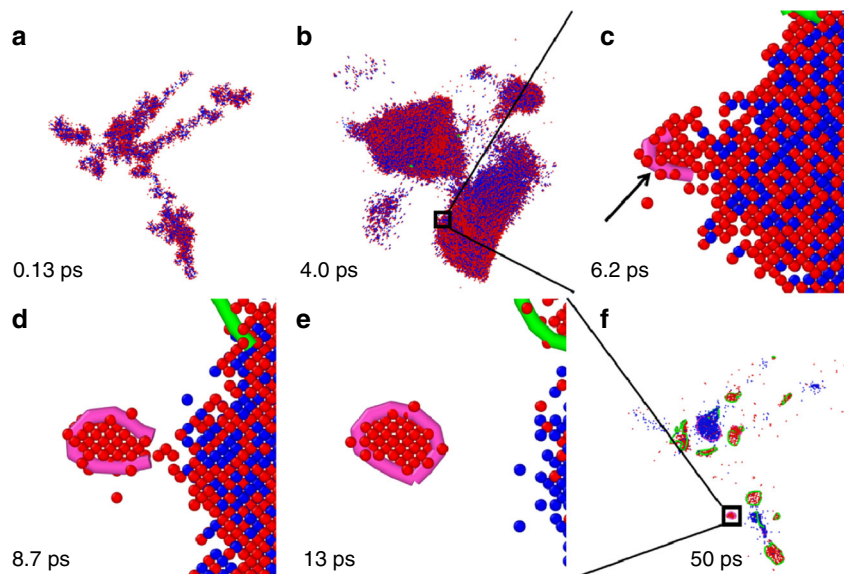


Fig. 1 Punch-out procedure. A primary knocked-on atom with the kinetic energy of 200 keV at time zero moves along the $\langle 351 \rangle$ direction to initiate the cascade, with sequence of **a** subcascade, **b** thermal spike, **c** $\langle 100 \rangle$ interstitial dislocation loop nucleation, **d** formation, and **e** stabilization in the zoom-in region, and **f** the quenched stage. The snapshots are taken as side-views along the $\langle 010 \rangle$ direction of the cubic system, for better view of the $\langle 100 \rangle$ dislocation loops. Only the defects are displayed. The red particles stand for interstitial atoms and the blue particles are for vacancies. The black arrow is the eye-guide for the position of the nucleation of the $\langle 100 \rangle$ interstitial-type dislocation loops. The pink lines denote $\langle 100 \rangle$ dislocation loops and the green lines are for the $\langle 111 \rangle$ dislocation loops

loop, respectively, with loop perimeter 4.3 and 9.4 nm, and diameter of 1.4 and 3.0 nm, respectively. We trace the positions of these interstitial atoms with the advantage of MD simulations. The root-mean-square displacement (RMSD), referring to the position at time 0 (right before the collision), is displayed in Fig. 2a as a function of time for both the $\langle 100 \rangle$ loop and the $\langle 111 \rangle$ loop. The large portion of displacement ($>95\%$) completes in a very short time, about 2 ps for both loops. After that, the interstitial atoms only process local rearrangement, without much change in their positions. The snapshots of the interstitial atoms composing the $\langle 100 \rangle$ loop are projected to a (110) plane as the insets. These interstitial atoms are punched out and ejected within a couple of picoseconds. Then the $\langle 100 \rangle$ loop formed after local relaxation without much change of their positions. The $\langle 111 \rangle$ loop starts moving earlier, but the final RMSD is less than that of the $\langle 100 \rangle$ loop. It is also reflected in the inset of Fig. 2c, where the $\langle 111 \rangle$ loop (green) is closer to the collision centre (blue) than the $\langle 100 \rangle$ loop.

The shockwave strength is associated with the atoms' velocity. The root-mean-square velocity (RMSV) is a measure of the average velocity of an object, which is obtained directly from time derivative of the root-mean-square displacement. The nucleation of the $\langle 111 \rangle$ interstitial loop initiates at 0.049 ps. With the supersonic wave generated from the collision, all the 108 interstitial atoms gain the RMSV as high as 3.72 km s^{-1} at 0.074 ps. The nucleation of the $\langle 100 \rangle$ loop starts a little bit later at 0.09 ps, but the 40 interstitial atoms forming the $\langle 100 \rangle$ loop gain a higher RMSV of 4.89 km s^{-1} at 0.132 ps. This high RMSV reflects the dislocation formation mechanism that is punched out by shockwaves. After the punch, the RMSV quickly reduces to 0.1 km s^{-1} , indicating the loops experience thermal vibrations thereafter, consistent with the picture of their positions. The dynamic procedure of the shockwave generating dislocation loops is also illustrated in Supplementary Movie 2.

It is worth noting that the mechanism for dislocation generation in shockwave deformation has been proposed 40 years ago³¹. It is well accepted that shock compression introduces homogeneous nucleation of dislocations in crystals³². Here the

shockwaves generated in the displacement cascade are localized, heterogeneous, and complicated because of the subcascades: multiple shockwaves are generated during the process at the time scale of picoseconds and length scale of nanometres.

Both the $\langle 100 \rangle$ and the $\langle 111 \rangle$ loops nucleate in the same collision, sharing the same depleted zone (blue region in the inset of Fig. 2c). One might be curious about the fundamental rule that determines the types of these shockwave induced dislocation loops. To that end, we examine the energies of the selected $\langle 100 \rangle$ and $\langle 111 \rangle$ interstitial loops. The kinetic energies of interstitial atoms in the loop are summed up at each time step during the cascade. The average kinetic energies are elucidated in Fig. 2c for both the $\langle 100 \rangle$ and the $\langle 111 \rangle$ loops. The maximum mean kinetic energy of the $\langle 100 \rangle$ loop is 3.5 eV per atom at the time of 0.132 ps, and the counterpart of the $\langle 111 \rangle$ loop is 2.0 eV per atom at the time of 0.074 ps. During the cascade, the nucleation of interstitial dislocation loops includes two parts: the generation of interstitials (vacancies) first and then formation of the loop. Therefore, the formation energy of the interstitial dislocation loops from a pure crystal system should also include the formation of vacancies and the interstitials. The vacancy formation energy is 1.718 eV, agreeing with the experimental value measured by positron annihilation³³. With a scaling value of the formation energy of interstitial loops²⁰, the total formation energy is 4.14 eV and 3.94 eV per atom for the $\langle 100 \rangle$ loop and the $\langle 111 \rangle$ loop, respectively (Fig. 2c). It is evident that the punch provides enough kinetic energy to form the $\langle 100 \rangle$ loop within high energy cascade. On the contrary, the average kinetic energy gained during the punch is not sufficient for the nucleation of a $\langle 100 \rangle$ loop, resulting the nucleation of the $\langle 111 \rangle$ loop instead (Fig. 2c).

It is worth pointing out that the average kinetic energy is more than that needed to form the $\langle 100 \rangle$ loop as shown in Fig. 2c. One might expect that the nucleation of the $\langle 100 \rangle$ interstitial loop could occur in a lower PKA recoil energy. We later confirm that one individual $\langle 100 \rangle$ interstitial loop nucleates in $E_{\text{PKA}} = 150 \text{ keV}$ cascades. However, we have not observed the nucleation of individual $\langle 100 \rangle$ interstitial loops for all 10 cascades simulations

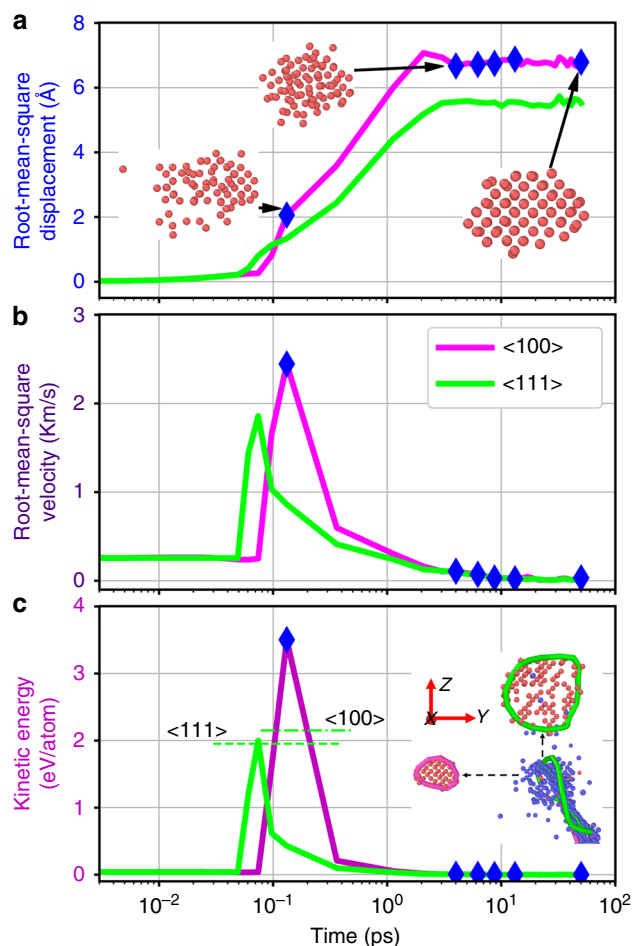


Fig. 2 Punch-out mechanism. One $\langle 100 \rangle$ (red) and one $\langle 111 \rangle$ (green) interstitial loop are selected for analysis of their **a** the root-mean-square displacement, **b** root-mean-square velocity, and **c** averaged kinetic energy per atom as a function of time for the interstitial atoms forming the dislocation loops. The insets in **a** show the morphology of the SIA atoms consisting of the $\langle 100 \rangle$ loop at three different stages. The blue diamond dots mark the corresponding locations in the curves for the snapshots in Fig. 1. The dash-lines in **c** mark the formation energies of the dislocation loops per atom. The selected $\langle 100 \rangle$ and $\langle 111 \rangle$ interstitial loops are in the inset of **c** with coordination orientation. The red dots denote the interstitial atoms and the blue dots denote the vacancies. The $\langle 100 \rangle$ loop and $\langle 111 \rangle$ loop are represented by the red and green lines, respectively

with the PKA recoil energy of 100 keV. It is well known that the morphology and the distribution of the debris are very complex^{27–29} due to the subcascade formation and the occurrence of channelling, in addition to the anisotropic nature of crystal structure. As a result, a deterministic redistribution of the injected PKA energy is impossible. The cascade procedure differs from case to case in stochastic nature. In fact, we have done 10 cases of displacement cascades of the same PKA recoil energy and temperature but on different PKA atoms and directions (all along $\langle 351 \rangle$ directions). Only 7 out of 10 cases have the individual $\langle 100 \rangle$ interstitial dislocation loops nucleated. As a comparison, it is 1 and 0 out of 10 cases for $E_{\text{PKA}} = 150$ and 100 keV, respectively. Coincidentally, the energy cutoff in observation of $\langle 100 \rangle$ interstitial loops in this study agrees with the experiments, as the first report of the $\langle 100 \rangle$ interstitial loops in iron also utilized 150 keV Fe^+ ion irradiation⁶.

Obviously, increase of the PKA recoil energy can augment the probability of the nucleation of $\langle 100 \rangle$ interstitial loops. Since the

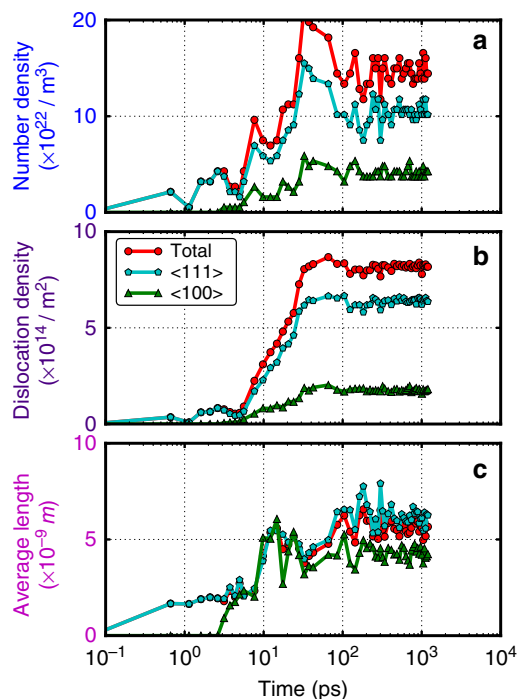


Fig. 3 Dislocation density. **a** The number density; **b** Density; **c** Average length of the dislocations of $\langle 100 \rangle$ and $\langle 111 \rangle$ types and total as a function of time

kinetic energy provides the main source of generating $\langle 100 \rangle$ interstitial loops, the increase of the efficiency of kinetic energy transfer during the collision is another way to enlarge the nucleation probability of $\langle 100 \rangle$ interstitial loops. This could be achieved by the heavy ion bombardment means surface interaction. Actually, by artificially increasing the PKA atom mass, a recoil energy as low as 20 keV have been reported to generate $\langle 100 \rangle$ interstitial loop in a MD study³⁴. The reason is that the large mass makes the velocity smaller for the same kinetic energy, leading to smaller damage volume and high kinetic energy density, which in turn boosts the nucleation of the $\langle 100 \rangle$ interstitial loops. In other words, the efficiency and population of the $\langle 100 \rangle$ loops could be tuned by the PKA recoil energy and the incident ion mass or species.

One might be concerned with whether the formation of $\langle 100 \rangle$ interstitial loops described above is an artefact of the interatomic potential used. To check that, we repeat the displacement cascade simulations using M07³⁵, M11², and Ackland04³⁶ potentials. In all potentials, the $\langle 100 \rangle$ interstitial loops were observed in cascade simulations with $E_{\text{PKA}} = 200$ keV. Therefore, the punch-out mechanism for the nucleation of $\langle 100 \rangle$ interstitial loops in high energy displacement cascades of 200 keV in iron is not limited to the Mendelev potential we used.

After punch-out. Besides the nucleation, the growth and evolution of microstructures are important in governing the materials' properties. There are about 56 dislocation loops nucleated in the cascade shown in Fig. 1, including both vacancy loops and interstitial loops, $\langle 111 \rangle$ and $\langle 100 \rangle$ types, full loops and segments. The dislocation number density (number of dislocations per volume), dislocation density (total dislocation length per volume) and the average length of dislocations are displayed in the panel of Fig. 3a–c respectively, as a function of time. The number densities have a much larger fluctuation before 100 ps and reach a plateau thereafter. The number density ratio of $\langle 111 \rangle$ to $\langle 100 \rangle$ loops is about 2.5:1. The $\langle 111 \rangle$ dislocation loops are dominant

with about three times more than the <100> loops. The individual dislocation loop might change length and positions after nucleation. However, the dislocation densities are quite conservative in our MD simulation time up to 1200 ps. Referring to the number density curves, the dislocation density ones are much smoother, and they are stable after 100 ps. The dislocation density of <111> loops takes 78.3% of the total, meaning that the ratio of <111> to <100> loops is about 4:1. The average length of the dislocation loops is 5.6, 6.3, and 4.3 nm for total, <111> and <100> loops, respectively, in this case. The average length of <100> loop in our studies is smaller than that of <111> loops and the diameter is 1.4 nm.

In addition to the fundamental understanding of displacement cascade that we discussed above, this proposed punch-out mechanism could have interesting and promising applications. The sessile <100> loops are immobile compared to the <111> loops due to the much higher formation energy and migration barrier. As a result, it can serve as an additional sink to point defects and enhance the recombination with the vacancies, while the <111> loops can be quickly absorbed by grain boundaries and dislocations due to their small migration energies. Therefore, more vacancies will be eliminated during the recombination process, effectively reducing the swelling. For the same reason, with the enhanced recombination of interstitials and vacancies, the embrittlement will be reduced with less defects. Therefore, it might be a feasible avenue to fabricate advanced steels with high resistance to both swelling and hardening by engineering the <100> dislocation loops via high energy particle bombardment, heavy-ion implantation³⁷, laser shock, and other shock loadings.

Discussion

In summary, through large-scale molecular dynamics simulations of high energy displacement cascades, we have observed the nucleation of <100> interstitial dislocation loops. Based on the velocity and energy analysis, we propose the punch-out mechanism of the formation of <100> interstitial dislocation loops through supersonic shockwaves, which is directly nucleated within a few picoseconds during displacement cascade. The new mechanism provides more insight in engineering microstructures via ion implantation, high energy particle bombardment, or shockwave compression.

Methods

Molecular dynamics simulations. The classical molecular dynamics simulations are carried out using the Large-scale Atomic/Molecular Massively Parallel Simulator (LAMMPS)³⁸, accompanying with the embedded-atom-method (EAM) empirical potential^{39,40} for atomic interactions. We choose this potential because it provides correct description of the relative stability of SIAs of different configurations and the vacancy migration energy. The universal screened-Coulomb potential was employed to describe the short-range (<0.1 nm) interatomic interaction in high-energy atomic collisions in cascades. In the middle range (from 0.10 to 0.20 nm), the interatomic interaction is a hybrid of the two potentials by an exponential spline.

Large simulation boxes of $200a_0 \times 200a_0 \times 200a_0$, $384a_0 \times 384a_0 \times 384a_0$, and $480a_0 \times 480a_0 \times 480a_0$ in bcc structure containing 16,000,000, 113,246,208, and 221,184,000 iron atoms, respectively, are used for the classical molecular dynamics simulations of the high energy displacement cascade at temperature of 300 K. a_0 is the lattice constant with the value of 0.287 nm. The side length of the cubic MD simulation box is 57.3, 110.2, and 137.8 nm, respectively. The size effect was examined comparing to a larger simulation box of $384a_0 \times 384a_0 \times 384a_0$ with 113,246,208 atoms and the side length is 110 nm. The PKA recoil energies of 100, 150, and 200 keV are examined.

Prior to initiating the cascade, a block was equilibrated for 40 ps at 300 K. This initial atom block was then used as a starting point for the cascade simulation and a reference for the defect analysis. The cascade was initiated by imparting a kinetic energy E_{PKA} to the selected primary knock-on atom (PKA) along a high-index direction. To avoid channelling by the PKA, a high-index direction <135> was used. Integration of the equations of motion of atoms was performed using a leapfrog algorithm with variable time-step, determined by limiting the displacement of the fastest atom to $0.0166a_0$ in one time-step. This number is carefully selected as the long time (40 ps) average of the maximum displacement of

simulation system with 16,000,000 iron atoms after thermodynamical equilibrium before the cascade simulations.

No electronic stopping or electron-phonon coupling was included in the simulations. Zarkadoula et al. employed a two-temperature model to study the effect of electronic stopping on defect production in bcc iron^{29,41,42}, and reported that there is no substantial difference in defect generation with and without electronic stopping for the recoil energies ranged from 200 to 500 keV²⁹. In addition, it has been noted that the electron-phonon coupling has no substantial effect on the final damage for examined recoil energies of 100 and 200 keV in bcc iron⁴¹. Furthermore, there is a parameter, known as cutoff kinetic energy, for electronic stopping in MD modelling. A value of 5.4 km s^{-1} or higher is generally adopted for iron^{41,42}, which is higher than the shock speed of 4.89 km s^{-1} for a <100> loop formation. Therefore, considering the electronic energy loss will not significantly change our main conclusions.

All results were obtained in the micro-canonical ensemble (NVE), with periodic boundary conditions. The NVE boundary conditions are well examined. The boost of the instantaneous temperature and pressure is 13.9 K and 0.048 GPa, respectively, at the thermal spike stage, which is negligible. The variation of temperature and pressure of the system as a function of time during a displacement cascade are illustrated in Supplementary Figure 1 and Supplementary Figure 2, respectively. The long-range elastic strain has negligible effect on the generation of the <100> interstitial loops in our model. The Wigner-Seitz defects were calculated using Voronoi cell analysis⁴³ in OVITO⁴⁴. The dislocation analysis were performed using OVITO⁴⁵. These settings have successfully employed in previous displacement cascade studies.

Data availability

The data that support the findings of this study are available in Mendeley Data with the identifier <https://doi.org/10.17632/pk5kktvdb5.1>

Received: 23 January 2018 Accepted: 9 October 2018

Published online: 16 November 2018

References

- Arakawa, K. et al. Observation of the one-dimensional diffusion of nanometer-sized dislocation loops. *Science* **318**, 956–959 (2007).
- Proville, L., Rodney, D. & Marinica, M. Quantum effect on thermally activated glide of dislocations. *Nat. Mater.* **11**, 845–849 (2012).
- He, B. B. et al. High dislocation density-induced large ductility in deformed and partitioned steels. *Science* **357**, 1029–1032 (2017).
- Coleman, R. V. Observations of dislocations in iron whiskers. *J. Appl. Phys.* **29**, 1487–1492 (1958).
- Carrington, W., Hale, K. & Mclean, D. Arrangement of dislocations in iron. *Proc. R. Soc. A* **259**, 203 (1960).
- Masters, B. C. Dislocation loops in irradiated iron. *Nature* **11**, 254 (1963).
- Eyre, B. L. & Bartlett, A. F. An electron microscope study of neutron irradiation damage in alpha-iron. *Philos. Mag.* **12**, 261–272 (1965).
- Masters, B. C. Dislocation loops in irradiated iron. *Philos. Mag.* **11**, 881–893 (1965).
- Dudarev, S. L., Bullough, R. & Derlet, P. M. Effect of the α/γ phase transition on the stability of dislocation loops in bcc iron. *Phys. Rev. Lett.* **100**, 135503 (2008).
- Yao, Z., Jenkins, M. L., Hernández-Mayoral, M. & Kirk, M. A. The temperature dependence of heavy-ion damage in iron: a microstructural transition at elevated temperatures. *Philos. Mag.* **90**, 4623–4634 (2010).
- Schaubl, R., Décamps, B., Prokhorodtseva, A. & Löffler, J. F. On the origin of primary $1/2\alpha_0 < 111 >$ and $\alpha_0 < 100 >$ loops in irradiated Fe(Cr) alloys. *Acta Mater.* **133**, 427–439 (2017).
- Soned, N. & de la Rubia, T. D. Defect production, annealing kinetics and damage evolution in $\alpha\text{-Fe}$: an atomic-scale computer simulation. *Philos. Mag.* **78**, 995–1019 (1998).
- Marian, J., Wirth, B. D. & Perlado, J. M. Mechanism of formation and growth of $\alpha < 100 >$ interstitial loops in ferritic materials. *Phys. Rev. Lett.* **88**, 255507 (2002).
- Eyre, B. L. & Bullough, R. On the formation of interstitial loops in b.c.c. metals. *Philos. Mag.* **12**, 31–39 (1965).
- Xu, H., Stoller, R. E., Osetsyky, Y. N. & Terentyev, D. Solving the puzzle of $\alpha < 100 >$ interstitial loop formation in bcc iron. *Phys. Rev. Lett.* **110**, 265503 (2013).
- Arakawa, K., Amino, T. & Mori, H. Direct observation of the coalescence process between nanoscale dislocation loops with different Burgers vectors. *Acta Mater.* **59**, 141–145 (2011).
- Tapasa, K., Barashev, A. V., Bacon, D. J. & Osetsyky, Y. N. Computer simulation of the interaction of carbon atoms with self-interstitial clusters in alpha-iron. *J. Nucl. Mater.* **361**, 52–61 (2007).
- Chen, J., Gao, N., Jung, P. & Sauvage, T. A new mechanism of loop formation and transformation in bcc iron without dislocation reaction. *J. Nucl. Mater.* **441**, 216–221 (2013).

19. Zhang, Y., Bai, X.-M., Tonks, M. R. & Biner, S. B. Formation of prismatic loops from C15 Laves phase interstitial clusters in body-centered cubic iron. *Scr. Mater.* **98**, 5–8 (2015).
20. Alexander, R. et al. Ab initio scaling laws for the formation energy of nanosized interstitial defect clusters in iron, tungsten, and vanadium. *Phys. Rev. B* **94**, 24103 (2016).
21. Granberg, F., Byggmatar, J., Sand, A. E. & Nordlund, K. Cascade debris overlap mechanism of <100> dislocation loop formation in Fe and FeCr. *EPL* **119**, 56003 (2017).
22. Kang, C., Wang, Q. & Shao, L. Kinetics of interstitial defects in alpha-Fe: the effect from uniaxial stress. *J. Nucl. Mater.* **485**, 159–168 (2017).
23. Yang, L. et al. Enhanced formation of <100> and <111> interstitial loops by helium clustering in bcc iron. *Mater. Lett.* **190**, 260–262 (2017).
24. Terentyev, D., Malerba, L., Klaver, P. & Olsson, P. Formation of stable sessile interstitial complexes in reactions between glissile dislocation loops in bcc {F}e. *J. Nucl. Mater.* **382**, 126–133 (2008).
25. Sand, A. E., Dudarev, S. L. & Nordlund, K. High-energy collision cascades in tungsten: dislocation loops structure and clustering scaling laws. *EPL* **103**, 46003 (2013).
26. Chen, Y. et al. New interatomic potentials of W, Re and W-Re alloy for radiation defects. *J. Nucl. Mater.* **502**, 141–153 (2018).
27. Calder, A. F., Bacon, D. J., Barashev, A. V. & Osetsky, Y. N. On the origin of large interstitial clusters in displacement cascades. *Philos. Mag.* **90**, 863–884 (2010).
28. Setyawan, W. et al. Cascade morphology transition in bcc metals. *J. Phys. Condens. Matter* **27**, 225402 (2015).
29. Zarkadoula, E. et al. The nature of high-energy radiation damage in iron. *J. Phys. Condens. Matter* **25**, 125402 (2013).
30. Béland, L. K., Osetsky, Y. N., Stoller, R. E. & Xu, H. Interstitial loop transformations in FeCr. *J. Alloys Compd* **640**, 219–225 (2015).
31. Meyers, M. A. A mechanism for dislocation generation in shock-wave deformation. *Scr. Metall.* **12**, 21–26 (1978).
32. Bringa, E. M. et al. Shock deformation of face-centred-cubic metals on subnanosecond timescales. **5**, 805 (2006).
33. Kim, S. M. & Buyers, W. J. L. Vacancy formation energy in iron by positron annihilation. *J. Phys. F. Met. Phys.* **8**, L103 (1978).
34. Calder, A. F., Bacon, D. J., Barashev, A. V. & Osetsky, Y. N. Effect of mass of the primary knock-on atom on displacement cascade debris in α -Fe-iron. *Philos. Mag. Lett.* **88**, 43–53 (2008).
35. Marinica, M.-C., Willaime, F. & Crocombette, J.-P. Irradiation-induced formation of nanocrystallites with C15 laves phase structure in bcc iron. *Phys. Rev. Lett.* **108**, 25501 (2012).
36. Ackland, G. J., Mendelev, M. I., Srolovitz, D. J., Han, S. & Barashev, A. V. Development of an interatomic potential for phosphorus impurities in α -Fe-iron. *J. Phys. Condens. Matter* **16**, S2629–S2642 (2004).
37. Liu, X. et al. Ion-irradiation-induced microstructural modifications in ferritic/martensitic steel T91. *J. Nucl. Mater.* **490**, 305–316 (2017).
38. Plimpton, S. Fast parallel algorithms for short-range molecular dynamics. *J. Comput. Phys.* **117**, 1–19 (1995).
39. Bonny, G. et al. On the thermal stability of late blooming phases in reactor pressure vessel steels: an atomistic study. *J. Nucl. Mater.* **442**, 282–291 (2013).
40. Terentyev, D., Zinovev, A. & Bonny, G. Displacement cascades in FeNiMnCu alloys: RVP model alloys. *J. Nucl. Mater.* **475**, 132–139 (2016).
41. Zarkadoula, E. et al. Electronic effects in high-energy radiation damage in iron. *J. Phys. Condens. Matter* **26**, 085401 (2014).
42. Zarkadoula, E., Samolyuk, G. & Weber, W. J. Two-temperature model in molecular dynamics simulations of cascades in Ni-based alloys. *J. Alloy. Compd.* **700**, 106–112 (2017).
43. Rycroft, C. H., Grest, G. S., Landry, J. W. & Bazant, M. Z. Analysis of granular flow in a pebble-bed nuclear reactor. *Phys. Rev. E* **74**, 21306 (2006).
44. Stukowski, A. Visualization and analysis of atomistic simulation data with OVITO—the Open Visualization Tool. *Model. Simul. Mater. Sci. Eng.* **18**, 15012 (2010).
45. Stukowski, A., Bulatov, V. V. & Arsenlis, A. Automated identification and indexing of dislocations in crystal interfaces. *Model. Simul. Mater. Sci. Eng.* **20**, 85007 (2012).

Acknowledgements

We would like to acknowledge the generous financial support from SNERDI-UOM project. Computational resources for LAMMPS calculations were provided by Rensselaer Polytechnic Institute through AMOS, the IBM Blue Gene/Q system at the Centre for Computational Innovations. The data analysis was partially performed using computation resources provided by High-Performance Computing Centre, Wuhan University.

Author contributions

F.G., L.W. and S.D. designed the project. Q.P., F.M., Y.Y., and H.D. performed the simulations. Q.P., F.G., C.L., and H.D. performed the analysis. Q.P. wrote the paper. All authors discussed and commented on the manuscript.

Additional information

Supplementary Information accompanies this paper at <https://doi.org/10.1038/s41467-018-07102-3>.

Competing interests: The authors declare no competing interests.

Reprints and permission information is available online at <http://npg.nature.com/reprintsandpermissions/>

Publisher's note: Springer Nature remains neutral with regard to jurisdictional claims in published maps and institutional affiliations.



Open Access This article is licensed under a Creative Commons Attribution 4.0 International License, which permits use, sharing, adaptation, distribution and reproduction in any medium or format, as long as you give appropriate credit to the original author(s) and the source, provide a link to the Creative Commons license, and indicate if changes were made. The images or other third party material in this article are included in the article's Creative Commons license, unless indicated otherwise in a credit line to the material. If material is not included in the article's Creative Commons license and your intended use is not permitted by statutory regulation or exceeds the permitted use, you will need to obtain permission directly from the copyright holder. To view a copy of this license, visit <http://creativecommons.org/licenses/by/4.0/>.

© The Author(s) 2018